Received 29 July 2025; revised 11 September 2025; accepted 27 September 2025. Date of publication 14 October 2025; date of current version 24 October 2025.

Digital Object Identifier 10.1109/OJCOMS.2025.3620865

EM Simulation, Implementation and Performance Evaluation of a Varactor-Based Reconfigurable Intelligent Surface

JOKIN CIFUENTES (Member, IEEE), IBAN BARRUTIA (Member, IEEE), AND MIKEL MENDICUTE (Senior Member, IEEE)

Electronics and Computer Science Department, Mondragon Unibertsitatea, 20500 Mondragón, Spain

CORRESPONDING AUTHOR: J. CIFUENTES (e-mail: jcifuentes@mondragon.edu)

This work was supported by the Department of Education of the Basque Government through its Research Group Program under Grant IT1451-22.

ABSTRACT Reconfigurable Intelligent Surfaces (RIS) are passive antenna arrays capable of dynamically modifying their reflective properties to adapt to variations in the communication channel by adjusting the reflection coefficient of each unit cell. RIS technology has attracted significant attention for its potential to enhance wireless communication systems, with envisioned applications in smart cities, indoor environments, and 5G/6G networks, enabling more reliable and adaptive communications. This paper presents the design, simulation, implementation, and validation of an RIS operating at 9.6 GHz, composed of a 40×40 array of unit cells, where reconfiguration is achieved using Barium Strontium Titanate (BST) varactors in combination with a clustering strategy that groups five unit cells under a single control element. This approach reduces the number of independent finite elements and control lines by 80%, with a quantified worst-case performance loss of 1.72 dB. As a first step, material properties and physical phenomena such as mutual coupling between adjacent unit cells and surface edge effects were investigated through full-wave simulations. Additionally, the S-parameters of the varactor models were incorporated into the simulations to apply programmable phase shifts across the surface, while statistical variations due to component tolerances were also considered to model realistic performance degradation. The designed surface was subsequently fabricated and experimentally validated, demonstrating strong correlation between measured and simulated results. A comparison between the deactivated and activated states of the RIS shows a reflection gain improvement exceeding 20 dB across the angular range from 20° to 80°. Finally, the proposed RIS was thoroughly evaluated through both electromagnetic simulations and comparisons with idealized theoretical models, offering valuable insights into practical performance degradation and reinforcing the importance of comprehensive performance evaluations under real-world hardware constraints.

INDEX TERMS Reconfigurable intelligent surface (RIS), sixth-generation (6G), EM simulation, experimental validation, hardware design.

I. INTRODUCTION

THE FIFTH-GENERATION (5G) network is currently being deployed worldwide, with full deployment expected by the end of 2025 [1]. However, both academia and industry are already looking beyond, focusing on Beyond 5G (B5G) and Sixth-generation (6G) technologies, which are being developed to meet increasingly demanding requirements, such as ubiquitous coverage, higher efficiency, ultra-high data rates, and extremely high reliability with lower latency [2].

According to a study by a leading technology company [3] applications such as mobile holography, digital twins, and immersive virtual reality are expected to be among the most prominent use cases of 6G networks. Deploying these applications requires performance levels that far exceed those of 5G. As illustrated in Fig. 1, there is a significant

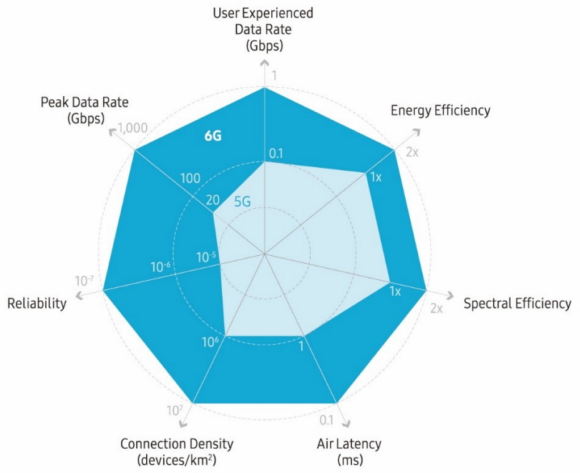

FIGURE 1. 5G (White) vs. 6G (Blue) requirements comparative [3].

performance gap between the capabilities of 5G and the stringent requirements of 6G. This gap has been widely discussed in the literature [4], highlighting the challenges of meeting these stringent demands with current 5G technologies and prompting the search for new solutions.

To address these demanding requirements, Reconfigurable Intelligent Surfaces (RIS) have emerged as a promising technology for 6G networks. RIS are two-dimensional structures composed of many unit cells. By adjusting the impedance of each individual cell, the collective response of the surface can be manipulated to control the reflected beam, enabling signal steering in the desired direction [5]. The technology is based on the concept of metasurfaces, which are artificially engineered materials whose properties are derived from internal micro/nano-structures, allowing them to control and manipulate electromagnetic (EM) waves [6]. These structures can modify EM wave properties in ways that are unachievable with natural materials [7]. However, it is important to note that traditional metasurfaces have a fixed response, meaning they cannot be reconfigured once fabricated.

RIS technology has attracted significant attention due to its potential to enable intelligent and reconfigurable environments for B5G/6G wireless systems. By incorporating electronically controllable components alongside dedicated control circuitry, RIS can dynamically adjust their reflection characteristics in response to changes in the communication channel [8], [9].

Most existing RIS studies have focused on evaluating the theoretical potential of the technology, typically analyzing key performance metrics such as signal-to-noise ratio (SNR) [8], [10], communication capacity in line-of-sight (LOS) and non-line-of-sight (NLOS) scenarios [5], and overall energy efficiency [11]. However, these analyses often rely on idealized mathematical models that overlook practical factors such as material properties and electromagnetic interactions that may arise in realistic implementations. As a result, electromagnetic simulations are essential to provide more accurate assessments of RIS behavior under realistic conditions. Furthermore, validating these simulations through physical prototyping and experimental measurements is critical for assessing practical feasibility and real-world performance.

In the area of reconfigurability, most studies focus on the use of discrete electronic components, primarily PIN diodes and varactor diodes. These devices are widely employed due to their ability to dynamically control the reflective properties of the unit cells, enabling phase and amplitude manipulation of the reflected signals. PIN diodes are typically used in binary switching schemes, allowing for on/off control of the reflective surface geometry [12], or by adding/removing different metal sections in the unit cell to create different phase shifts [13]. Varactor diodes, on the other hand, offer greater flexibility by providing continuous tuning range of capacitance and, consequently, more precise phase shifts [14].

A. RESEARCH OBJECTIVES

While numerous studies have demonstrated the theoretical benefits of RIS, few have addressed practical design, fabrication, and experimental validation. Existing experimental prototypes are predominantly based on PIN diodes. For instance, a 24×24 RIS composed of PIN-diode-based unit cells was designed, simulated, and fabricated in [15]. Similarly, in [13], two 16×16 RIS prototypes were implemented using five PIN diodes per unit cell, achieving a 2-bit configuration per cell. In contrast, studies involving reconfigurable unit cells based on varactor diodes are comparatively scarce. In [16], the electromagnetic behavior of unit cells using a single varactor diode was analyzed through full-wave simulation, but no system-level implementation was considered. A more advanced configuration using two varactors per unit cell to enhance phase control was explored in [17]; however, that study remained limited to simulation, without addressing fabrication or experimental validation.

Among the existing literature, many works—particularly those involving varactor-based reconfigurability—are restricted to full-wave electromagnetic simulations of individual unit cells or entire surfaces, without progressing to physical implementation or experimental validation under real operating conditions. A few experimental demonstrations can be found, such as a RIS operating at 5.8 GHz, where each unit cell employed two varactors to achieve only 1-bit phase reconfiguration [18], and another RIS at 5.25 GHz requiring four varactors per unit cell to implement phase tuning [19]. These approaches rely on more than one varactor per unit cell, which not only increases the total number of components required to implement the RIS, but also demands multiple biasing lines per cell, thereby complicating the overall reconfiguration process. Moreover, while such designs may be suitable at relatively low frequencies—where the unit cell size is large enough to integrate several varactors—the need for multiple

components becomes increasingly problematic at higher frequencies, where unit cells must be significantly reduced in size in proportion to the wavelength.

B. NOVELTY AND ADVANTAGES OF THE PROPOSED RIS DESIGN

To fill this gap, this work focuses on the design and implementation of a varactor-based RIS composed of a 40×40 array of unit cells. The rationale behind these dimensions will be discussed later in the paper. Nevertheless, the proposed design is scalable, enabling the development of larger RIS structures if required. In contrast to prior varactor-based implementations, the proposed approach relies on a 2-bit phase configuration with a single varactor per unit cell, thereby simplifying the unit cell design compared to previous studies and offering a viable solution for implementations at higher frequencies. To further reduce the complexity of the reconfiguration process without compromising functionality, the unit cells were grouped into clusters, thereby reducing even further the number of components and control lines. The entire development process was conducted through EM simulations to accurately characterize the unit cells, determine the most efficient clustering strategy, and evaluate the overall RIS performance. Finally, the designed surface was fabricated and experimentally validated, with its performance compared to studies analyzing SNR under idealized RIS models.

Beyond these improvements over existing varactor-based designs, the proposed approach also introduces important benefits compared to PIN-diode-based RIS prototypes, especially in the context of future high-frequency systems. First, from a physical perspective, the varactor diodes used in this work feature a smaller footprint (0.5 mm × 0.25 mm) than the smallest commercially available PIN diodes (0.6 mm × 0.3 mm, such as those used in [15]). This miniaturization becomes increasingly important as the operating frequency rises, since the unit cell size decreases proportionally.

Moreover, while multi-bit phase quantization with PIN diodes requires at least $log_2(N)$ diodes per unit cell—meaning that at least two diodes are needed for 2-bit (four-phase) control—varactor-based designs can achieve equivalent functionality using a single component. By applying different bias voltages, a single varactor can generate the required discrete impedance states for 2-bit phase modulation.

Another key distinction lies in the reconfiguration strategy. PIN-diode-based RIS systems inherently perform on/off switching at the individual unit cell level, since their operation relies on electrically connecting or disconnecting specific metallic sections within each unit cell. Consequently, such designs do not readily support clustering approaches. In contrast, the continuous tuning capability of varactor diodes enables cluster-based reconfiguration schemes, where multiple unit cells are grouped under a common control signal.

Finally, the proposed design also demonstrates significant advantages in terms of power consumption, achieving a reduction of more than two orders of magnitude compared to a representative PIN-diode-based prototype, as analyzed in detail in Section IV.

C. CONTRIBUTIONS

The main contributions and results of this paper are summarized below:

- This paper provides detailed information on the design and simulation of a RIS, where unit cell reconfiguration is achieved by grouping cells into clusters, with a single varactor diode used to control each cluster. This design choice reduces the number of independent finite elements and control lines by 80%, with a corresponding reflectivity reduction of approximately 33% at $\theta_r = 20°$ and 24% at $\theta_r = 60°$. BST varactors are employed to adjust the impedance of the clusters, offering wide tuning ranges (up to 60%), approximately 10% component tolerances, and switching speeds close to 150 ns. For more realistic results, the S-parameter models of the varactors, including statistical tolerance distributions, were incorporated into the EM simulations. This approach enabled modeling of manufacturing tolerances as a normal distribution and evaluating their impact on RIS performance through Monte Carlo simulations, providing insights into the robustness and reliability of the proposed design under manufacturing variability.
- The various challenges associated with the simulation setup and fabrication of the RIS were identified and analyzed. Effects such as mutual coupling between neighboring cells, surface edge effects, and the material properties used were carefully considered in the EM simulations. Furthermore, details of the fabrication process using Printed Circuit Board (PCB) technology were examined, highlighting important factors to ensure practical implementation.
- The designed RIS was fabricated and validated in a measurement setup, demonstrating strong correlation between simulated and measured results, thus confirming the feasibility of the design. To ensure realistic performance assessment, the simulations also incorporated the varactor tolerances, modeling their impact on gain degradation and steering accuracy. Moreover, the reflection gain achieved with the RIS in its active state—where the surface is configured to steer the reflected beam towards the desired angle—was compared to its inactive state, where it acts as a conventional metallic reflector with a normal incidence response. This comparison revealed a reflection gain improvement exceeding 20 dB across the entire angular range from 20° to 80°.
- Comparisons were made between ideal RIS simulation results from other studies and the more realistic results obtained in this work, including both EM simulations and experimental measurements. By evaluating the

communication capacity achieved with a physically implemented RIS, this study provides a more accurate assessment of practical performance compared to idealized models. Additionally, it highlights the importance of considering the reflection angle in capacity calculations, as reflection efficiency decreases with increasing reflection angles.

The rest of the paper is organized as follows. Section II introduces the key concepts related to RIS technology. Section III describes the EM simulation setup and the characterization process of the unit cells, including the methods and tools used. The design and simulations of the unit cells, the clusters, and the complete RIS are presented in Section IV. Section V presents the validation setup and the results obtained from the implemented RIS. In Section VI, a comparison of the achievable communication capacity with the RIS is presented, contrasting the EM simulation and experimental results of this study with those from related works assuming ideal RIS responses. Section VII presents the conclusions and outlines potential directions for future research.

II. KEY CONCEPTS

The functionality of reconfigurable intelligent surfaces is based on three key concepts: The generalized Snell's law, the isotropy of the elements composing the surface, and the discretization given to the unit cells.

The generalized Snell's law has been analyzed in several studies [20], [21]. This law states that, in order to reflect a signal incident on a surface at an angle θ_i (measured from the surface normal) to a reflection angle θ_r, it is necessary to apply a phase gradient $(d\phi(x)/dx)$ across the surface, as described by the following equation:

$$\sin\theta_r - \sin\theta_i = \frac{\lambda_0}{2\pi n_1}\frac{d\phi(x)}{dx}. \tag{1}$$

Observing (1), it can be seen that to obtain specular reflection ($\theta_i = \theta_r$), the phase gradient to be applied is 0. However, to achieve an anomalous reflection ($\theta_i \neq \theta_r$), it is necessary to apply a phase gradient on the surface $(d\phi(x)/dx \neq 0)$. Fig. 2 shows the phase gradients that must be applied by the surface to reflect a $\theta_i = 0°$ wave at different values of θ_r. Note that the slope becomes steeper as the difference between incidence and reflection angle increases. This requires greater precision in applying the desired phase, as the phase difference between adjacent cells becomes smaller, which in turn leads to a degradation of the surface's reflective response as this angular difference increases.

The isotropic nature of the unit cells is the basis for the operation of these structures. These surfaces are composed of a large number of sub-wavelength unit cells [22], as smaller cell sizes yield a more isotropic response [23].

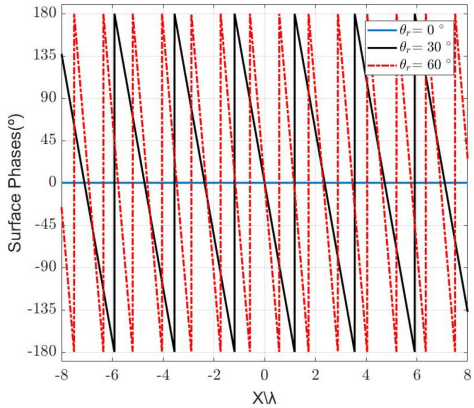

FIGURE 2. Phases to apply on the surface to generate the desired anomalous reflection with an incident wave $\theta_i = 0°$.

This can be understood by looking at (2) in [24], which is related to the magnitude of the scattered field in the far field (S):

$$S(r,\theta_s) = \left(\frac{bb}{\lambda}\right)^2 \frac{E_i^2}{r^2}\cos^2(\theta_i)\left(\frac{\sin(\frac{\pi b}{\lambda}(\sin(\theta_s)-\sin(\theta_i)))}{\frac{\pi b}{\lambda}(\sin(\theta_s)-\sin(\theta_i))}\right)^2, \tag{2}$$

where $S(r,\theta_s)$ represents the scattered electric field observed at a distance r and angle θ_s. The parameter b denotes the unit-cell size, while λ corresponds to the operating wavelength. The term E_i is the incident electric field illuminating the RIS, θ_i is the angle of incidence, and θ_s is the scattering angle.

Considering the case where the incidence and scattering observation angles are both 0° (i.e., $\theta_i = \theta_s = 0°$), the second and third terms of (2) equal unity. As a result, the scattered field simplifies to $S(r,\theta_s) = \left(\frac{bb}{\lambda}\right)^2$, which indicates that larger unit cells produce a higher magnitude of the scattered signal. However, when maintaining $\theta_i = 0°$ while allowing $\theta_i \neq \theta_s$, it is observed that for a large unit cell, an increase in the observation angle leads to a significant reduction in the magnitude of the reflected signal. This decrement is primarily attributed to the division by $\frac{\pi b}{\lambda}$ in the last term of (2). In contrast, when considering the same observation scenario with a much smaller (sub-wavelength) unit cell, the reduction in the reflected signal's magnitude is considerably less pronounced. This demonstrates that smaller unit cells exhibit higher isotropy, as they reflect signals with a lower overall magnitude than larger cells but with a more uniform intensity across all scattering angles.

The last key concepts is the discretization of the phase gradient. As mentioned above, a RIS is based on the application of phase gradients using sub-wavelength unit cells. This means that in order to implement a RIS, it is necessary to divide the theoretically continuous phase gradient among the unit cells that make up the surface, thus discretizing it. Therefore, predefined discretizations are used in the cells, usually with 1-bit quantization, which allows phase changes of 0° and 180°; or 2-bit quantization, which allows changes of 0°, 90°, 180° and 270° in the cells [25].

Several theoretical studies have analyzed the effect of quantizing the unit cell phases, concluding that the difference in SNR between a continuous phase shift and a 2-bit phase shift is 0.9 dB, whereas for a 1-bit phase shift, the difference is close to 3.9 dB [25], [26]. In addition, a previous study using fabricated metasurfaces verified that the difference between using a continuous phase shift and a 2-bit phase shift is minimal, 0.1 dB in the main reflection lobe [27]. It was also shown that the difference between applying a continuous phase shift and a 1-bit phase shift is approximately 3 dB. Furthermore, it was observed that the 1-bit phase discretization induces a diffraction lobe due to aliasing caused by the coarse phase quantization.

III. EM SIMULATIONS

The performance of the RIS is governed by the collective behavior of its constituent unit cells. Consequently, the accurate design and electromagnetic characterization of these cells—and their mutual interactions across the array—are critical for the synthesis and performance optimization of the RIS.

To account for practical implementation effects such as mutual coupling between adjacent elements, edge diffraction, conductor and dielectric losses, and other non-ideal factors, full-wave electromagnetic simulations were conducted using CST Studio Suite. In this framework, the unit cell response was analyzed using Floquet ports and appropriate boundary conditions, allowing its electromagnetic behavior to be characterized while considering the influence of surrounding periodic elements.

Floquet ports are based on Floquet's theorem, which states that the solution to a differential equation with periodic coefficients can be expressed as the product of a periodic function and a complex exponential [28]:

$$u(t) = e^{i\beta t}P(t), \tag{3}$$

where $P(t)$ is a periodic function with period T and β is the Floquet wavenumber representing the phase shift per period.

The simulation domain is bounded by appropriate conditions on each face of the computational box. Along the X and Y axes, *UnitCell* boundary conditions are applied to simulate infinite periodicity in-plane and capture coupling effects between neighboring elements. Along the Z-axis, an *Open*(*AddSpace*) condition is used. This condition extends the simulation domain in the vertical direction, providing additional space for the Floquet mode to propagate. As a result, the waves have more distance to travel before reaching the boundary, minimizing undesired reflections and enabling a more accurate representation of the interaction between the unit cell and the incident field. This simulation setup is illustrated in Fig. 3.

Following this setup, in [27], a comparison was made of the reflectivity obtained in a unit cell of size $\lambda/6 \times \lambda/6$ with different substrate materials for a center frequency of 9.6 GHz. Typical PCB technology substrates are compared based on the following parameters:

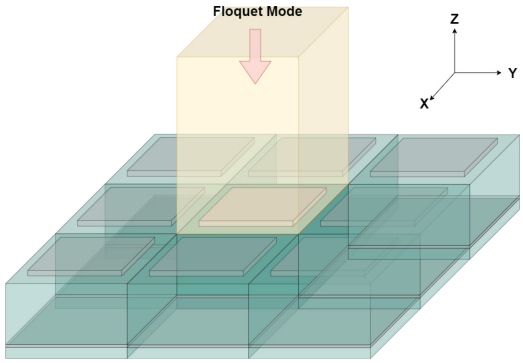

FIGURE 3. Unit cell configuration with eight identical surrounding cells along the X–Y axes, and open boundary conditions along the Z axis to allow wave propagation.

- *FR4:* $\epsilon_r = 4$ and $\tan(\delta) = 0.0195$ @1GHz
- *Isola MT40:* $\epsilon_r = 3.45$ and $\tan(\delta) = 0.0031$ @10GHz
- *Rogers RO4003C:* $\epsilon_r = 3.55$ and $\tan(\delta) = 0.0027$ @10GHz

The results show that the FR4 substrate cell has the lowest performance, with a reflectivity loss of nearly 1 dB compared to the other materials. This reduction is attributed to the material's losses ($\tan(\delta)$), which is approximately an order of magnitude greater than that of Isola MT40 and Rogers RO4003C. In contrast, the reflective responses obtained using Isola MT40 and Rogers substrates are nearly identical, due to their similar permittivities and low loss tangents. Both in [27] and in this work, Isola MT40 has been employed as the substrate material. While Rogers RO4003C offers slightly superior physical properties, these are not critical for the targeted operating conditions, making Isola MT40 a more cost-effective and suitable choice for this design.

IV. DESIGN

A. UNIT CELL

In a previous study [27], a unit cell was designed using a microstrip patch with two metal layers at the top and bottom, separated by a 1.5 mm thick substrate. To explore its behavior, the response of the cell was analyzed for different substrate materials. Additionally, it was observed that modifying the geometry of the top patch effectively altered its inductance and the capacitance between the layers, thereby adjusting the reactance of the unit cell's impedance and shifting its reflection phase. This demonstrated that, by correctly applying the generalized Snell's law to these structures, the direction of the reflected lobe could be controlled. Moreover, it provided insight into the gain loss in realistic hardware implementations compared to theoretical models.

Building upon this concept, instead of physically modifying the geometry of the unit cell, reconfigurability can be achieved through the integration of discrete electronic components. Two primary approaches for such reconfiguration have been widely reported in the literature. The first method utilizes PIN diodes [12], [13], which are

switched on or off by applying a bias voltage. This effectively connects or disconnects specific metallic sections of the unit cell to produce phase shifts by altering the physical geometry of the structure. The second approach involves varactor diodes [14], where reconfigurability is achieved by continuously adjusting the capacitance of the unit cell via bias voltage control, without any physical modification.

As discussed in Section I, varactor diodes offer several advantages over PIN diodes, particularly in terms of miniaturization, control flexibility, reconfiguration strategies, and power consumption. For these reasons, varactor diodes were selected for this design, enabling precise and continuous phase shift control by modifying the capacitance of the unit cell through applied voltage. Furthermore, the varactors used in this work are based on tunable dielectric materials, allowing capacitance variation by adjusting the dielectric properties. This approach provides significant benefits for fine-grained phase control in unit cells, as will be further analyzed in the following sections.

In addition to these functional advantages, power consumption is a crucial factor in the practical scalability of RIS systems. Unlike PIN-diode-based RIS designs, which require considerable DC power to sustain the on-state of their components, varactor-based designs consume negligible static power, with only minimal current drawn during capacitance tuning.

A comparison of the power consumption between the unit cell design presented in [15] and the varactor-based design proposed in this work has been carried out, assuming a reconfiguration rate of 1 kHz—equivalent to one tuning operation every millisecond. In the PIN-diode-based prototype, each unit cell employs two PIN diodes to achieve reconfigurability, with each diode requiring approximately 13 nW under forward bias. Since the bias current must be continuously supplied to maintain the on-state, this results in a constant power consumption of up to 26 nW per unit cell when both diodes are active.

In contrast, the power consumption of the varactor-based unit cells has been estimated using an equivalent RC circuit model, based on the electrical parameters provided by the manufacturer. Since varactors consume energy solely during transitions between capacitance states, their average power consumption is determined by the reconfiguration frequency. Assuming a reconfiguration rate of 1 kHz, the energy consumed per tuning event is approximately 166 nJ. Integrating this over one second results in an average power consumption of 166 nW per unit cell.

This substantial reduction not only enhances scalability but also simplifies the biasing network and minimizes thermal management requirements. Furthermore, the cluster-based reconfiguration strategy adopted in this work further reduces the effective control power required for the entire surface.

The physical implementation of the unit cell is based on a four-layer PCB structure designed to ensure manufacturability, mechanical integrity, and optimal electromagnetic performance. Fig. 4 illustrates the physical layout of the unit cell, which consists of a top metal patch, a first substrate layer, a middle metal patch serving as the ground plane, a second substrate layer, and a bottom metal layer where the connections and discrete electronic components are located. The structure consists of a 1.5 mm thick Isola-MT40 core with 17 µm copper foil on both the top and bottom surfaces. Below the core, a 0.1 mm prepreg of the same material is added to meet the microvia requirements, followed by another 17 µm copper foil layer.

During manufacturing, an additional 25 µm of copper is applied to both sides, resulting in a total thickness of 42 µm for the top and bottom metal layers. This additional copper is added by the PCB manufacturer to comply with standard fabrication tolerances and ensure reliability in the plating process. However, it does not adversely affect the electromagnetic performance of the unit cell. At the operating frequency of 9.6 GHz, the skin depth in copper is approximately 0.6654 µm, which means that most of the current is confined to a layer that thick—significantly smaller than the total 42 µm metal thickness. To confirm this, full-wave simulations were carried out, showing that the additional copper has no measurable impact on the unit cell's response.

The unit cell's structural dimensions and interconnections are as follows: the top metal patch measures 4 mm (L) $\times$ 4 mm with a thickness of 42 µm (t_1), while the core has dimensions of 5 mm (W) $\times$ 5 mm and a thickness of 1.5 mm (h_1). The middle metal layer measures 5 mm $\times$ 5 mm with a thickness of 17 µm (t_2), and the prepreg layer has the same dimensions with a thickness of 0.1 mm (h_2). To ensure proper electrical connectivity, vias are used: a plated-through hole (PTH) connects the top and bottom layers, passing through the core, ground plane, and prepreg, while also providing a pad to feed the varactor diode. Additionally, a microvia links the middle (ground) and bottom layers, passing through the prepreg and offering a ground pad for the varactor connection. Fig. 4c presents the physical representation of the bottom layer, highlighting the PTH and the microvia, as well as the pads for the varactor diode and the power lines.

B. CLUSTER

Generalized Snell's Law defines the phase gradient required on a surface to redirect an incident signal at a specific angle, with the gradient applied along a single axis. When the phase gradient is applied along the X-axis, the reconfiguration occurs vertically, causing the reflective lobe of the surface to shift in the vertical direction. Conversely, applying the phase gradient along the Y-axis results in horizontal reconfiguration, leading to a change in the reflective lobe's direction along the horizontal plane. Based on this principle, unit cells can be grouped into clusters along rows or columns,

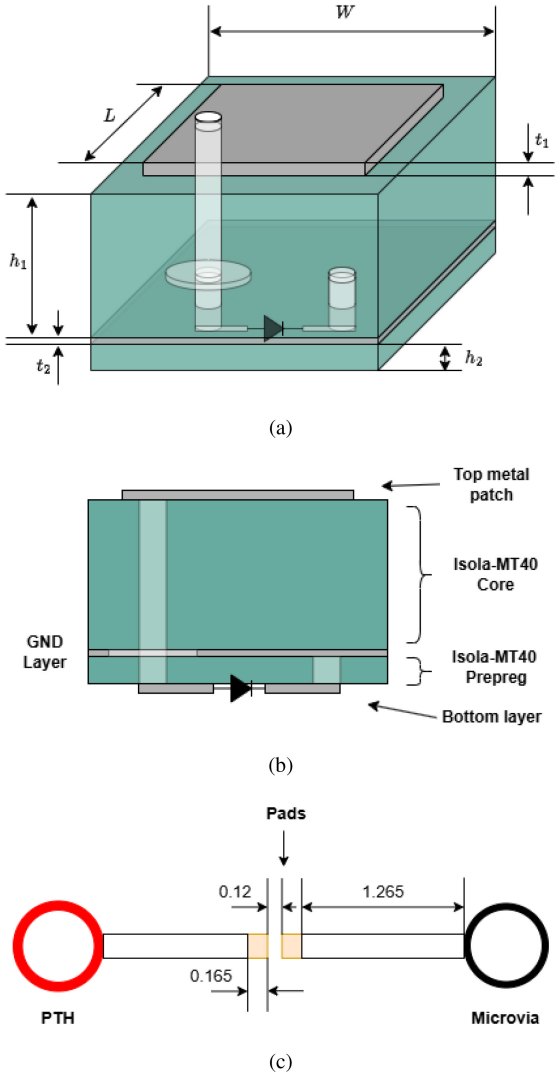

FIGURE 4. Physical representation of the unit cell. (a) Isometric view. (b) Front view. (c) Bottom view.

depending on the desired reconfiguration, ensuring uniform phase application within each cluster.

Clustering the cells enables the use of a single varactor and bias voltage to apply a uniform phase across all cells within each cluster, simplifying the overall architecture, reducing system complexity, and facilitating the reconfiguration process by allowing a single varactor to control the phase shift across multiple cells. The clustering approach was implemented specifically to make the reconfiguration easier, thus allowing for more straightforward measurements of the RIS in the validation setup.

While this clustering approach offers significant advantages in terms of simplicity and energy efficiency, it also presents certain limitations. A primary drawback is the reduced flexibility in reconfiguration. Although this limitation does not affect the application of Snell's Law, it becomes problematic when reconfiguring across both the X and Y axes, as individual phase control for each

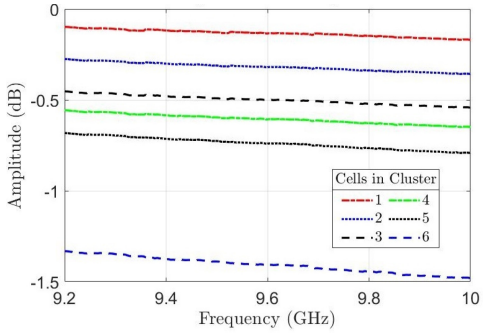

FIGURE 5. Average reflection coefficient by changing the number of cells in the cluster.

cell is not feasible. Another disadvantage is that as the number of cells in the cluster increases, the reflectivity of individual cells — and consequently the reflectivity of the entire cluster — decreases, as demonstrated in the electromagnetic comparison of Fig. 5, which presents the reflectivity measurements taken from clusters of varying cell numbers grouped vertically. For each configuration, the reflectivity was averaged over phase shifts of 0°, 90°, 180° and 270° applied to the cells. This approach provides the average reflectivity for each cluster under a 2-bit phase shift, revealing a trend where the reflectivity amplitude decreases as the number of cells increases. Considering these factors, this design groups the cells vertically, facilitating the application of the same phase across vertical clusters and allowing effective horizontal control of RIS reconfiguration. It can be observed that the loss increases monotonically with cluster size, with a pronounced gap when transitioning from a 5-cell to a 6-cell cluster. Assuming an acceptable threshold of 1 dB for reflection loss, the cells were therefore grouped into clusters of five in the initial design.

To further assess the impact of 5-cell clustering, a comparative analysis was performed between two versions of the RIS design proposed in this work: one without clustering and the other with 5-cell clustering. The analysis was conducted for reflection angles of $\theta_r = 20°$ and $\theta_r = 60°$, in order to evaluate the influence of clustering across the full operational range of the RIS, as analyzed in more detail later in the manuscript. As illustrated in Fig. 6, the results reveal a reflection amplitude reduction of approximately 1.7 dB at $\theta_r = 20°$, and about 1.2 dB at $\theta_r = 60°$. This trend is consistent with the observations in Fig. 5, where the use of clustering reduces the reflection coefficient amplitude of the unit cells, thereby decreasing the overall reflectivity of the RIS. Despite this reduction in reflection power, no significant differences were found in terms of beamforming precision or steering flexibility. Additionally, higher sidelobe levels were observed in the non-clustered RIS due to its increased reflectivity.

Given that the influence of the clustering approach only affects the reflection power — without compromising the

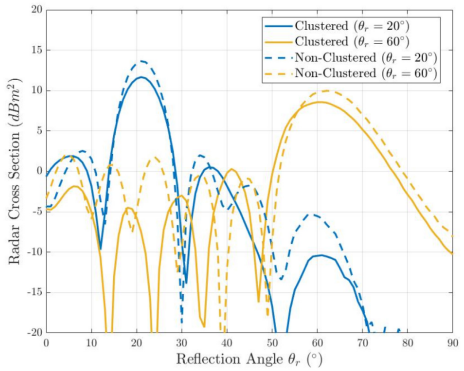

FIGURE 6. RCS comparison between Clustered and Non-Clustered RIS configurations for reflection angles $\theta_r = 20°$ and $\theta_r = 60°$.

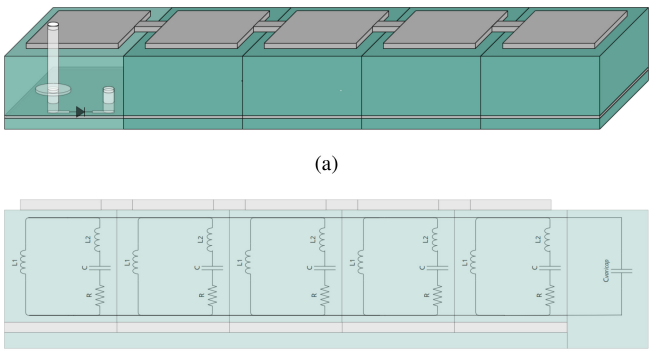

(a)

(b)

FIGURE 7. 5-cell cluster schematic. (a) Physical representation. (b) Equivalent electric circuit.

beam steering precision or flexibility — the final design adopts a 5-cell cluster configuration. This choice simplifies the surface design and improves system efficiency by allowing a single varactor diode to reconfigure five cells simultaneously. As a result, the number of independent finite elements and control lines is reduced by 80%, with a corresponding reflectivity reduction of approximately 33% at $\theta_r = 20°$ and 24% at $\theta_r = 60°$.

The cluster design is shown in Fig. 7. The top layer reflector patches are interconnected so that the varactor affects the impedance of each cell without affecting the overall response of the cluster. In addition, the varactor diode connection to the top metal patch has been strategically located along the lateral edge of the patch. This positioning is critical because the varactor must be located where the field variation is greatest to maximize its effect. Since the electric field is zero at the center of the patch and peaks at the edges, placing the varactor at the edges ensures proper integration into the system for optimal operation. The figure also shows the equivalent electrical circuit, where each of the cells consists of four electronic elements [29]:

- *L1:* Equivalent inductance of the metal ground plane.
- *L2:* Equivalent inductance of the metallic top patch.

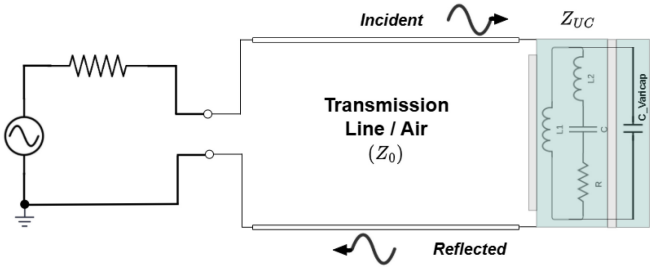

FIGURE 8. Equivalent circuit for the TL propagation model of a unit cell within the cluster.

- *C:* Equivalent capacitance of the lower and upper metal planes.
- *R:* Losses in the metals and dielectric of the unit cell.

On the other hand, there is a capacitance C_{Varicap} that affects all the cells, which refers to the capacitance generated by the varactor diode. The influence of the vias and pads is not shown due to their negligible impact, as confirmed through simulations.

Fig. 8 illustrates the equivalent circuit for the transmission line (TL) propagation model for an incident EM wave propagating through the air towards the unit cell within the cluster. Taking into account the reflection coefficient formula for a transmission line:

$$\Gamma = \frac{Z_{\text{L}} - Z_0}{Z_{\text{L}} + Z_0}, \tag{4}$$

where Z_0 represents the characteristic impedance of the medium (air) and Z_L the load impedance at the end of the TL, and considering the equivalent circuit formula for the unit cell:

$$\begin{aligned} Z_{\text{UC}} = \frac{1}{Y_{\text{uc}}} &= \frac{(j\omega L_1)\left(j\omega L_2 + R + \frac{1}{j\omega C}\right)}{j\omega L_1 + j\omega L_2 + R + \frac{1}{j\omega C}} + \frac{1}{j\omega C_{\text{Varicap}}} \\ &= \frac{(j\omega L_1)\left(j\omega L_2 + R + \frac{1}{j\omega C}\right)}{\left(j\omega L_1 + j\omega L_2 + R + \frac{1}{j\omega C}\right) + j\omega C_{\text{Varicap}}(j\omega L_1)\left(j\omega L_2 + R + \frac{1}{j\omega C}\right)}. \end{aligned} \tag{5}$$

it can be seen that the unit cell impedance ($Z_L = Z_{UC}$) is a complex value. As a result, the reflection coefficient (Γ) is also complex, having both amplitude and phase. By varying the capacitance of the varactor, the reactive part of the unit cell impedance changes, which in turn modifies primarily the phase, while also producing a secondary effect on the amplitude of the reflection coefficient, as later observed in the simulation results.

EM simulations were conducted to analyze the response of the 5-cell cluster as the varactor capacitance was varied. In an initial test, a capacitor was connected to observe how different capacitance values affected the response of the cells. The results indicated that a 2-bit phase shift could be achieved over a capacitance range of 0.163 pF to 0.09 pF, specifically: 0° with 0.163 pF, 90° with 0.149 pF, 180° with 0.135 pF, and 270° with 0.09 pF.

To obtain more realistic results after confirming that, according to simulations, fixed capacitance values could

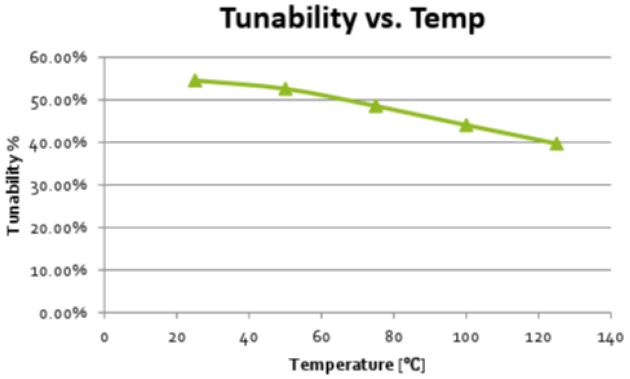

FIGURE 9. Tunability of the varactor as a function of temperature, based on manufacturer-provided characterization data.

effectively change the phase of the unit cells, S-parameter models of a Tecdia VB-type varactor were integrated into the EM simulations. These varactors are made of the ferroelectric material Barium Strontium Titanate (BST), which has an optimal Curie temperature, providing a low loss tangent and high thermal resistance [30]. The varactor allows for dynamic capacitance adjustment, ranging from 0.2 pF at 0 V to 0.08 pF at the maximum operating voltage of 20 V. In addition, the varactors have a tolerance of approximately 10% and a switching speed close to 150 nS [31]. Their low tolerance makes them a viable option for RIS applications, where precise capacitance control is essential for accurate phase shifting. Moreover, the high switching speed enables agile reconfiguration of the surface, which is particularly advantageous in vehicular environments or dynamic scenarios where real-time user tracking and fast beam steering are required.

In addition to the advantages mentioned above, the thermal behavior of the varactors must also be considered, as temperature variations can impact their tunability. Figure 9 shows the tunability of the varactors as a function of temperature, based on characterization data provided by the manufacturer. It can be observed that the tunability remains above 50% for temperatures below 60 °C, which is sufficient to cover the full phase tuning range required for the 2-bit configuration in each cluster. However, for deployments in more extreme environments, where temperatures may exceed 60 °C, a different unit-cell design would be required to guarantee 4-phase reconfigurability, as tunability is reduced at higher temperatures. One possible solution would be to employ a dual-varactor configuration, thereby extending the achievable capacitance range and maintaining the required tunability for full phase control.

After validating the tunability range and thermal stability of the varactors under typical operating conditions, Figure 10 presents the simulated reflective response of the 5-cell cluster, incorporating the S-parameter models of the VB-type varactors. Reflectivity losses remain below 1 dB across all configurations, while a 2-bit reconfiguration is successfully achieved across the cells.

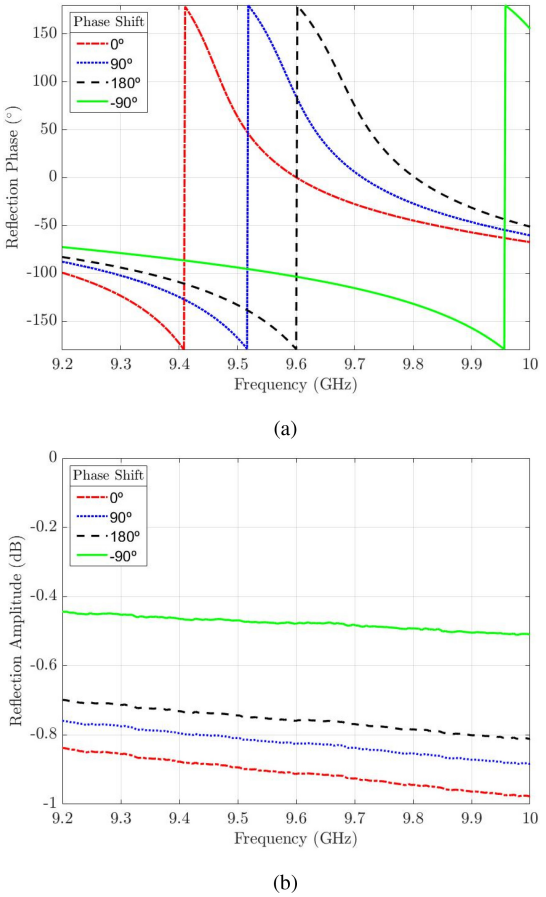

FIGURE 10. Reflective response of the 5-cell cluster when applying the S-parameter models of a VB type varactor. (a) Reflection coefficient phases. (b) Reflection coefficient amplitudes.

C. SURFACE

This subsection presents the design and results of the EM simulations of the RIS device. A 40x40 cell surface has been designed, with the elements grouped vertically in clusters of 5 cells (Fig. 11). These dimensions were chosen considering the operating frequency and the proper illumination of the surface within the measurement system. The operating frequency of 9.6 GHz was selected based on the available measurement equipment in the laboratory, which included horn antennas and a dedicated measurement kit for this frequency. Given the selected frequency, the unit cells were designed with dimensions of 5 × 5 mm (approximately $\lambda/6 \times \lambda/6$). Furthermore, considering the radiation pattern of the measurement antennas and the need to illuminate the RIS in the far field to effectively apply Snell's law to the structure, the overall surface size was chosen to be large enough to allow full illumination while avoiding excessive dimensions that would introduce implementation challenges and demand extensive time and simulation resources.

To optimize reconfiguration, the total reflection accounts for the response of all cells, but only 320 varactor diodes are used for reconfiguration, instead of the 1600 that would be required without clustering. Additionally, for horizontal

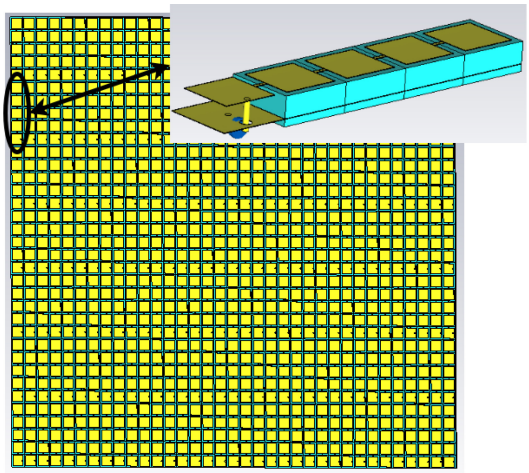

FIGURE 11. RIS design with a 5-cell cluster zoom in CST.

control of the surface, the control lines can be grouped into columns, reducing the number of required control lines to 40 (plus 5 ground lines). This grouping simplifies the measurement process in the validation setup by making reconfiguration more manageable. If reconfiguration of the RIS is needed along both axes, this can be achieved by foregoing the vias-line grouping in the design and directly controlling 320 lines, which remains a manageable solution. This would allow control of the main lobe in both axes; however, the fact that the cells are grouped into vertical clusters of 5 would result in a loss of some precision in the pointing accuracy.

The EM simulation results of the RIS are shown in Fig. 12. The surface is illuminated with a plane wave, which resembles a wave in the far-field, with an incident angle of $\theta_i = 0°$. Different phase gradients, calculated using the Generalized Snell's Law, are applied to the surface to obtain different reflection responses at various θ_r in the horizontal axis. As shown in the figure, the surface response can be manipulated by controlling the varactors' bias voltage, allowing the reflected signal direction to be steered. Fig. 12 also illustrates that as the difference between the angle of incidence and the desired reflection angle increases, the efficiency of the surface's reflection decreases. This phenomenon was discussed in [27] and is related to the isotropic response of the elements discussed in Section II.

To achieve more realistic results, the tolerances of the varactor have been incorporated into the RIS simulations. Considering a $\pm 10\%$ capacitance tolerance and assuming a normal distribution, a Monte Carlo simulation approach was employed to generate multiple RIS responses for reflection angles of 20°, 40°, 60°, and 80°, treating the capacitance variation as a random variable.

Table 1 summarizes the results, showing the RCS gains obtained without tolerances (in dBm^2), along with the worst-case gain losses observed when tolerances are applied. The table also includes the corresponding steering inaccuracies,

TABLE 1. Gain losses and steering inaccuracies due to tolerances.

Reflection Angle (°)	Gain (dBm^2)	Tol. Losses (dB)	Steering Inaccuracy (°)
20	11.67	1.457	±2
40	10.87	1.141	±3
60	8.567	0.839	±3
80	2.396	0.422	±6

defined as deviations in the main lobe direction. The observed gain reductions are primarily attributed to these angular deviations, as the main lobe is no longer centered precisely at the target reflection angle, leading to a decrease in the measured gain. Additional Monte Carlo simulations were carried out for two representative cases (20° and 60°), allowing for a more complete statistical perspective. The results indicate that the mean loss due to varactor tolerances is 1.1078 dB at 20°, and 0.668 dB at 60°.

At a reflection angle of 80°, the largest steering deviation is observed; however, the associated gain loss is minimal. This is explained by the broader radiation pattern at higher angles, which compensates for the steering error and reduces the impact on gain. As illustrated in Fig. 12, an increase in the reflection angle results in a wider main lobe, which mitigates the sensitivity of the system to angular tolerances.

V. EXPERIMENTAL VALIDATION

To validate the design and functionality of the proposed RIS, a prototype has been fabricated and assembled. The implemented RIS consists of a 40×40 array of unit cells, covering an area of 20 cm × 20 cm, identical to the simulated surface.

Fig. 13 shows the top and back views of the fabricated surface. The bottom of the board contains the 320 soldered varactors, as well as the control lines and a SFM connector. The control network consists of 45 traces: 40 dedicated to controlling each column of the RIS and 5 serving as ground lines. To ensure uniform distribution, ground lines are placed at regular intervals, every 10 control lines. The SFM connector is interfaced with a TFSS connector featuring the same number of pins. The cables from the TFSS are routed to a stripboard, which is equipped with eight 6-pin Phoenix terminals. This stripboard serves as an intermediate distribution interface for the control voltages required by the RIS. Figure 14 illustrates the stripboard with the eight soldered terminals and the cables from the TFSS connector connected to them.

The Phoenix terminals on the stripboard are wired to four independent power supplies, each configured with specific voltage values. These voltages are set to achieve the desired capacitance values in the varactors, ensuring the intended tunability of the RIS. Each couple of Phoenix terminals is connected to one of the four power supplies, resulting in 12 identical voltage lines for controlling the columns of the RIS. By adjusting the connections between the TFSS cables and the terminals, the voltage applied to each column can

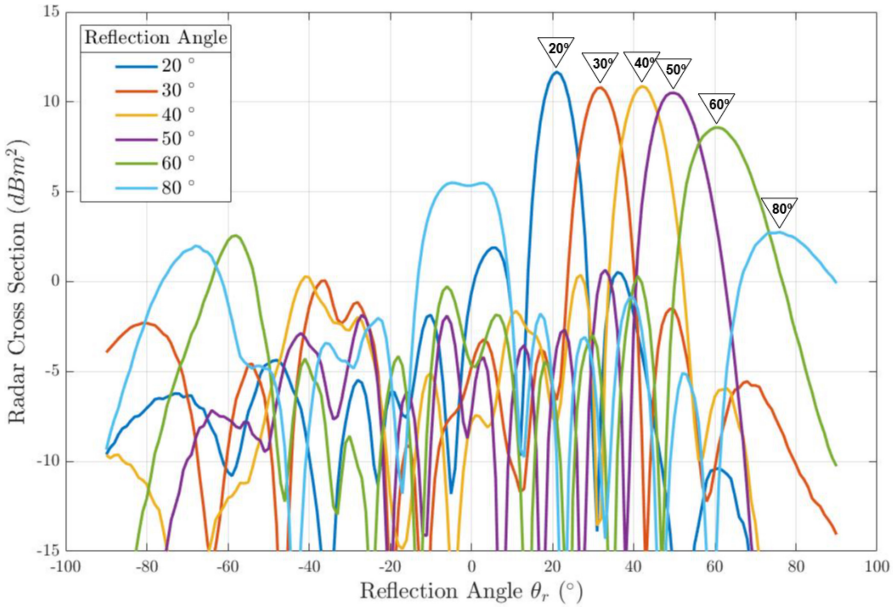

FIGURE 12. Simulated RIS responses for different reflection angles θ_r under normal incidence ($\theta_i = 0°$). The curves correspond to various target reflection angles θ_r as indicated in the legend.

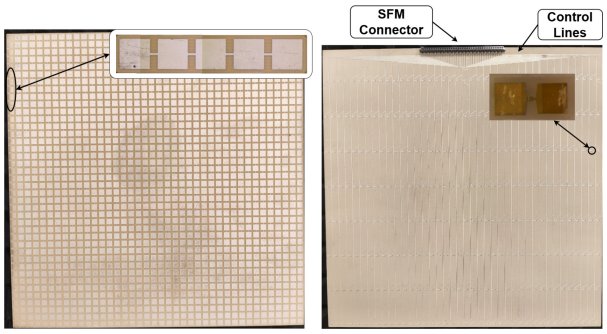

FIGURE 13. Fabricated prototype of the proposed RIS design. (a) Front view. (b) Back view.

be modified, enabling reconfiguration of the RIS response in accordance with the generalized Snell's law. However, the control of this surface could also be implemented using switches managed by a dedicated controller or an Field-Programable Gate Array (FPGA), maintaining the same power supply architecture while regulating the switches (and, therefore, the power supply to each column) through a controller, which would additionally enable scalability among identical RISs.

The measurement setup used to evaluate the performance of the fabricated RIS, specifically to characterize its reflection properties, is depicted in Fig. 15. Two horn antennas (Oritel ANC 100/15) have been used for the 8.5-9.6GHz band with a gain of 15 dB, one as the transmitter (Tx) and the other as the receiver (Rx). The Tx antenna is connected to a Gunn diode oscillator, which is powered by a dedicated power supply. This oscillator generates a signal at 9.6 GHz, matching the operating frequency of the RIS. The Rx antenna

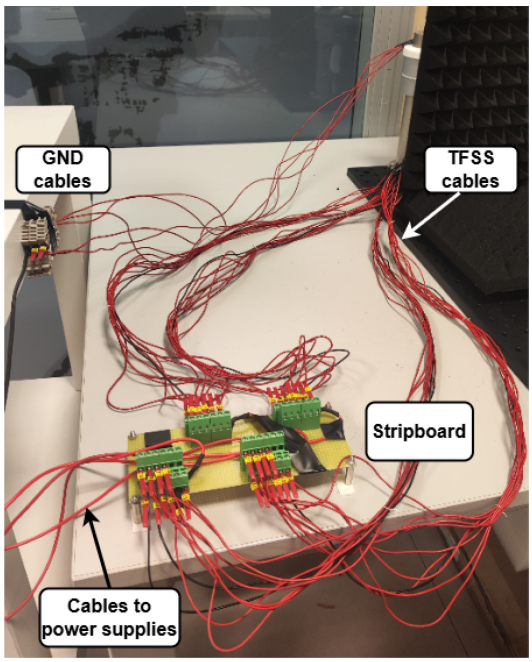

FIGURE 14. Control circuitry of the RIS system.

is directly connected to a spectrum analyzer, which allows measuring the power of the signal reflected by the RIS.

The Tx antenna remains fixed throughout the measurements and is positioned 0.4 m away from the RIS at an incidence angle of 0°, a configuration selected to ensure both far-field operation and full illumination of the metasurface without significant power loss. The minimum far-field distance is given by:

$$R_{\text{far-field}} = \frac{2D^2 f}{c}, \tag{6}$$

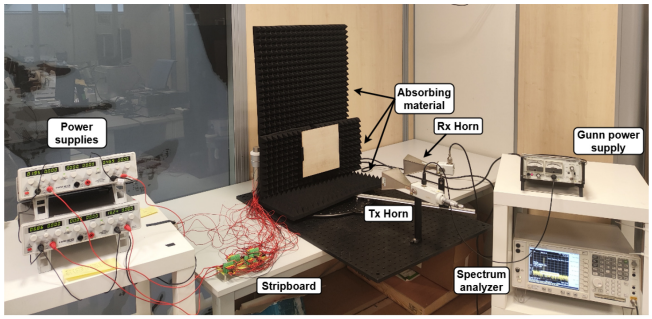

(a)

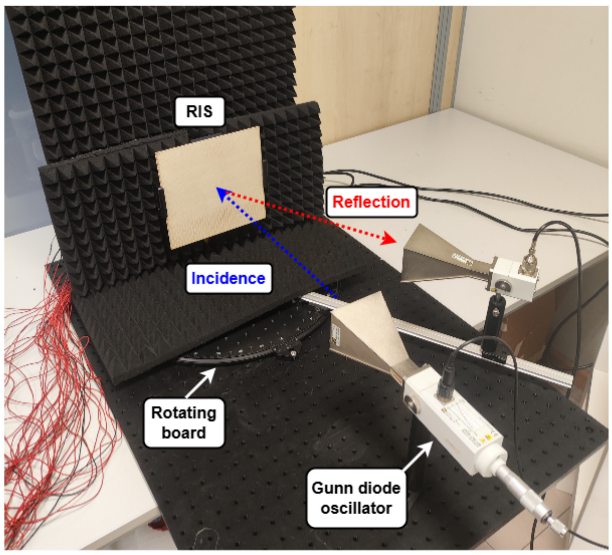

(b)

FIGURE 15. Setup used for RIS measurement and validation. (a) Overall measurement setup. (b) Detailed measurement scheme between horn antennas and RIS.

$D = 80$ mm is the largest aperture dimension of the horn antenna (80 mm $\times$ 68.5 mm), $f = 9.6$ GHz is the operating frequency, and c is the speed of light. This yields a minimum far-field distance of approximately 0.4 m.

Additionally, this distance ensures that the main lobe of the horn antenna fully covers the RIS. The minimum required distance for full illumination is calculated as:

$$d = \frac{R_{\text{covered}}}{\tan(\theta/2)}, \tag{7}$$

where $R_{Covered} = 0.1$ m (half the width of the RIS) and $\theta = 30°$ is the beamwidth of the horn antenna. This results in a minimum illumination distance of approximately 0.37 m, confirming that the 0.4 m setup satisfies both the far-field and illumination requirements.

In contrast, the Rx antenna is movable and scans different reflection angles. It is mounted on a circular rotating board, which is connected to a rail system that ensures precise positioning and is manually adjusted. The Rx antenna is also placed 0.4 m away from the RIS and is moved in 1° increments to capture the reflected power distribution. To minimize unwanted reflections from the metallic components of the measurement system, three absorbers have been placed: two behind the RIS and one underneath it.

TABLE 2. Measured reflection gains between inactive and active RIS states for different steering angles.

Reflection Angle (°)	Measured Gain (dB)
20	25.87
30	25.36
40	31.18
50	30.55
60	21.93
80	21.14

To assess the performance of the fabricated RIS, Fig. 16 presents a comparative analysis between the simulated and measured relative amplitude response at reflection angles of 20°, 30°, 40°, 50°, 60°, and 80°, with the corresponding discretized phase pattern shown as an inset in each plot to illustrate the surface configuration used to achieve the desired reflection angle. The relative amplitude response is defined as the measured reflected amplitude normalized to the maximum reflection obtained when the RIS is in its inactive state, where the surface reflects the incident wave specularly with normal reflection ($\theta_i = \theta_r = 0°$). This normalization provides a reference to evaluate how the RIS alters the reflected amplitude under different phase configurations, allowing for a quantifiable comparison between the measured and simulated responses. Additionally, Fig. 16a also includes the measured antenna-to-antenna coupling curve, normalized in the same way, which remains consistently below –30 dB across the reflection angles of interest, confirming that antenna coupling does not affect the RIS validation results, while only becoming noticeable beyond 80°, outside the range considered in this study.

From the results, it is observed that as the reflection angle increases, the amplitude also decreases. In this regard, the maximum peak is found at 22° ($\theta_r = 20°$) with a relative amplitude of −1.52 dB, −3.02 dB at 32° ($\theta_r = 30°$), −3.12 dB at 44° ($\theta_r = 40°$), −3.42 dB at 50° ($\theta_r = 50°$), −5.92 dB at 60° ($\theta_r = 60°$, and −10.62 dB at 76° ($\theta_r = 80°$).

Furthermore, to better quantify the enhancement achieved by the RIS, Table 2 summarizes the measured reflection gains between the inactive and active states for different steering angles. These values represent the difference in reflected amplitude when the RIS is reconfigured to steer the beam towards the desired angle, compared to its inactive state, in which the surface operates as a conventional metallic reflector with a normal-incidence response ($\theta_i = \theta_r = 0°$), functioning as a conventional metallic reflector. As shown, the RIS consistently provides reflection gains exceeding 20 dB across the entire steering range, with maximum gains exceeding 30 dB for the angles of $\theta_r = 40°$ and $\theta_r = 50°$.

For a global comparison, Fig. 17 consolidates all measured and simulated radiation patterns into a single plot.

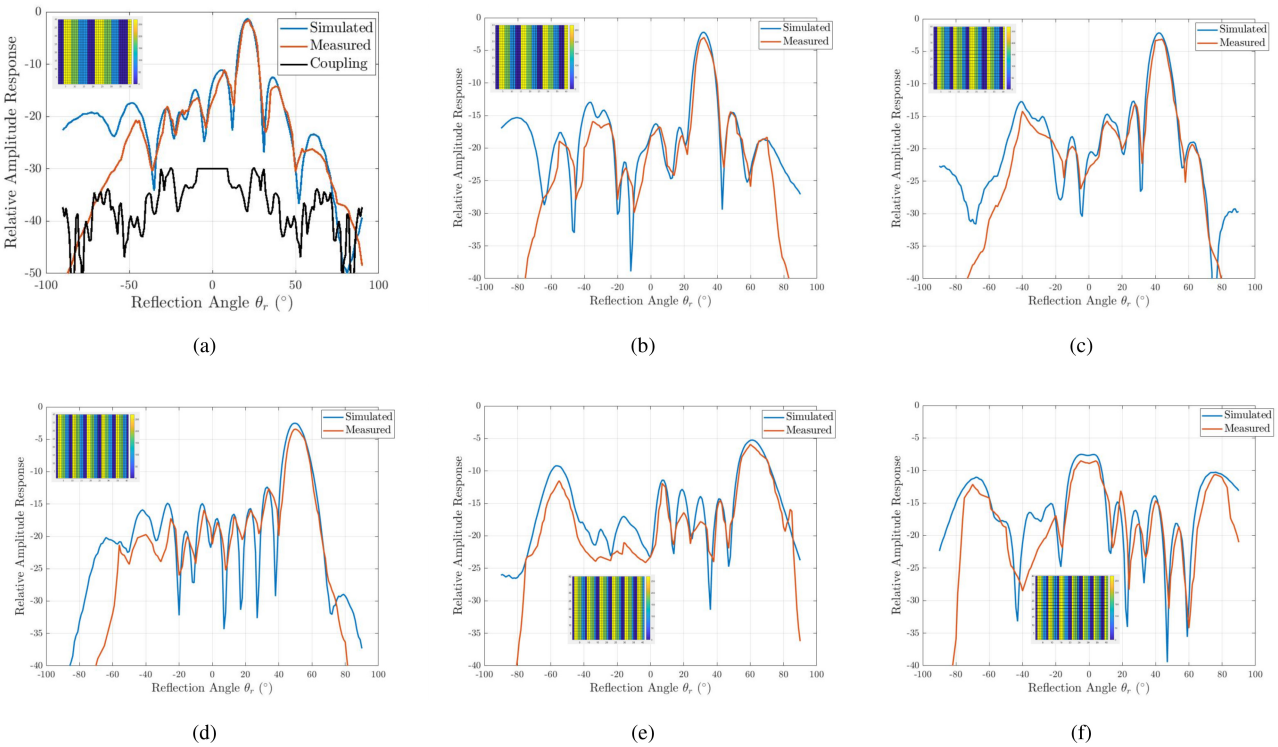

FIGURE 16. Comparison of simulated and measured RIS reflection patterns for different reflection angles, along with the discretized phase pattern applied to the surface. (a) $\theta_r = 20°$. (b) $\theta_r = 30°$. (c) $\theta_r = 40°$. (d) $\theta_r = 50°$. (e) $\theta_r = 60°$. (f) $\theta_r = 80°$.

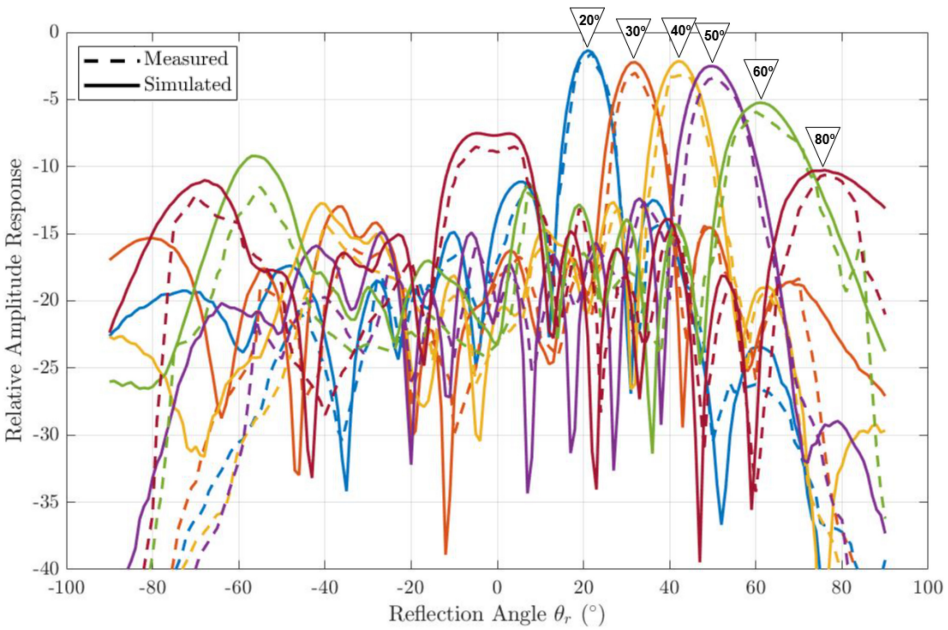

FIGURE 17. RIS response for different θ_r at $\theta_i = 0°$ incidence.

VI. PERFORMANCE METRICS AND COMPARISON WITH RELATED WORKS

In study [5], significant advancements were made in understanding the effectiveness of RIS in assisting wireless communications that may be blocked or require higher receiver power. The study evaluates RIS-assisted channel performance by assuming ideal phase application and a four-phase shift configuration in each unit cell, with each unit cell being perfectly reflective ($|\Gamma| = 1$). The analysis covers both LOS and NLOS scenarios, showing that RIS has a significantly greater impact on NLOS communications, particularly in assisting channels that are blocked or where LOS power

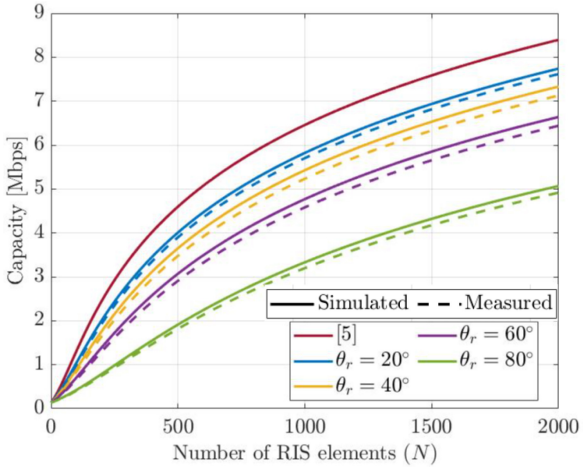

FIGURE 18. Comparison of an ideal 2-bit RIS with the simulated and measured results at different θ_r of this work.

is low. This impact is directly related to improvements in channel capacity, as RIS enhances the quality and reliability of the signal. Additionally, the difference in performance between using the ideal phase shift and a practical 2-bit phase configuration is minimal. However, relying on perfect reflectivity in the cells does not accurately represent real-world conditions, impacting the practical utility of RIS.

In this study, a comparison has been made between the electromagnetic simulation results and those from [5], as well as with the RIS measurement results obtained from the validation setup. Channel capacity has been compared at different reflection angles, as RIS reflectivity decreases when the difference between the angle of incidence and the angle of reflection increases.

Fig. 18 presents a comparative analysis of the capacity calculations between [5] and those obtained in this work, where the capacity has been computed for a bandwidth of 1 MHz, as in [5]. The study considers the multiple paths between the transmitter, the RIS cells, and the receiver, assuming that each cell has a gain of 1 ($|\Gamma| = 1$) and applies phase shifts of 0°, 90°, 180° or 270° (2-bit reconfiguration). As the number of cells increases, the number of in-phase paths summed at the receiver also rises, resulting in an increase in channel capacity. Equation (8) presents the SNR formula used in [5] for calculating the capacity in such a communication scenario, where $\alpha_n = -80$ dB, $\beta_n = -60$ dB and ρ represents direct communication gain between the transmitter and the receiver, with a value of $\rho = -110$dB, indicating NLOS communication

$$SNR = \frac{P}{BN_0}\left|\sqrt{\rho} + \sum_{n=1}^{N}\sqrt{\alpha_n\beta_n\gamma}\right|^2. \quad (8)$$

In contrast, this study calculates capacity by considering both the radiation patterns obtained from the simulations and those measured during the structure validation in the experimental setup. SNR is calculated as the sum of the channels between the transmitter and the RIS, the RIS and the receiver, and the gain of the RIS at different reflection angles, as shown in (9). This method provides a more accurate assessment of the capacity that reflects the actual performance of the RIS in practical communication scenarios

$$SNR = \frac{P}{BN_0}\left|\sqrt{\rho} + \sqrt{\alpha\beta G_{RIS}}\right|^2. \quad (9)$$

Fig. 18 also presents a comparison of the channel capacity as the number of RIS elements increases. The highest rates are observed with the ideal RIS, where each element reflects perfectly, and the reflection angle is not considered. This implies that communication capacity remains constant regardless of the user's position. Below this ideal case, eight additional capacity curves are shown, corresponding to different reflection angles (20°, 40°, 60°, and 80°). As the reflection angle increases, the capacity values decrease due to the reduced RIS gain at higher reflection angles, indicating lower efficiency in redirecting electromagnetic signals. This highlights the importance of considering user location in RIS-assisted communications.

VII. CONCLUSION AND FUTURE LINES

This work presents the design, simulation, implementation, and experimental validation of a Reconfigurable Intelligent Surface (RIS) operating at 9.6 GHz, consisting of a 40×40 array of unit cells. Reconfiguration is achieved using Barium Strontium Titanate (BST) varactor diodes, which provide a wide tunability range and low tolerances, enabling efficient impedance control. To further improve scalability and reduce hardware complexity, a clustering strategy is employed, grouping five unit cells under a single control element. This approach reduces the number of independent control lines and finite elements by 80%, while limiting the reflectivity reduction to approximately 33% at $\theta_r = 20°$ and 24% at $\theta_r = 60°$. A strong correlation has been achieved between simulated and experimental results, with reflection gain improvements exceeding 20 dB across the 20° to 80° steering range. Although the gain at 60° drops by more than 40% compared to 20°, the RIS continues to outperform the inactive state, maintaining high reflection efficiency even at steeper angles. The study also highlights, through comparison with other works, the importance of accounting for the reflection angle and the performance degradation associated with practical hardware implementations, reinforcing the need for realistic performance evaluations under non-ideal conditions.

The obtained results open new research directions for further advancements in RIS technology. Future work could focus on implementing adaptive reflection angle control through an FPGA device and evaluating the system's capacity in dynamic or mobile environments. To achieve this, the current manual bias tuning system would need to be replaced by a digital control scheme based on a microcontroller or FPGA. This would require modifying the current power distribution circuit, which is based on Phoenix terminal blocks, by replacing it with a digitally controlled

switching circuit capable of delivering four different analog bias levels to each column.

In the implemented RIS, which consists of 40 columns of clusters, each column could be addressed using a dedicated analog switch. This approach would require a total of 40 analog switches, with each switch controlled by two digital output signals from the FPGA to select among four predefined bias voltages. Therefore, the entire RIS could be dynamically controlled using an FPGA with at least 80 digital output pins, which is feasible with many commercial high-performance devices, such as those from the Xilinx Virtex family.

Regarding dynamic scenarios, FPGAs are capable of extremely fast digital signal switching, with typical propagation delays below 10 ns. Therefore, the overall reconfiguration speed of the RIS is mainly limited by the switching time of the analog switches—typically around 30 ns—and the response time of the BST varactors, which can reach up to 150 ns in the worst case. These values yield a total reconfiguration latency of approximately 180 ns, enabling update rates of up to 5.5 MHz and making real-time adaptation in fast-changing environments feasible.

Another promising avenue is the scalability of multiple identical RIS units, enabling a mosaic-like deployment to extend coverage and improve system performance. This approach would consist of replicating the RIS implemented in this work and arranging several panels either horizontally or vertically. Such a configuration would increase the overall reflectivity of the system, enabling stronger and more directive beamforming capabilities through coordinated operation.

Under manual control, such a multi-panel configuration would require additional Phoenix terminals for controlling the surfaces, proportionally increasing the number of control interfaces. It is important to note that, even when composed of discrete panels, the entire mosaic would function as a single RIS and therefore require a continuous phase gradient applied across the full structure.

This mosaic configuration could also be extended to dynamic reconfiguration using the column-based control approach proposed in this work. For instance, with an FPGA providing 640 digital output pins—a value achievable with high-performance FPGAs from families such as Xilinx Virtex or similar devices—it would be possible to independently control up to eight identical RIS panels, enabling large-scale coordinated operation while maintaining fast and centralized adaptability.

Finally, given the size and functionality of BST varactors, this design could be adapted to operate at higher frequencies, further expanding its potential applications in next-generation wireless networks.

REFERENCES

[1] M. Flinders, "The future of 5G: What to expect from this transformational technology." 2024. [Online]. Available: https://www.ibm.com/think/insights/5g-future

[2] N. Rajatheva et al., "White paper on broadband connectivity in 6G," 2020, *arXiv:2004.14247*.

[3] J. Doe, *Samsung's 6G White Paper Lays Out the COmpany'S VIsion for the NExt GEneration of COmmunications TEchnology*, Samsung, Suwon-si, South Korea, 2020.

[4] S. Zhang, Q. Wu, S. Xu, and G. Y. Li, "Fundamental green tradeoffs: Progresses, challenges, and impacts on 5G networks," *IEEE IEEE Commun. Surveys Tuts.*, vol. 19, no. 1, pp. 33–56, 1st Quart., 2017.

[5] E. Björnson, H. Wymeersch, B. Matthiesen, P. Popovski, L. Sanguinetti, and E. de Carvalho, "Reconfigurable intelligent surfaces: A signal processing perspective with wireless applications," *IEEE Signal Process. Mag.*, vol. 39, no. 2, pp. 135–158, Mar. 2022.

[6] N. Yu and F. Capasso, "Flat optics with designer metasurfaces," *Nat. Mater.*, vol. 13, pp. 139–150, Jan. 2014. [Online]. Available: https://api.semanticscholar.org/CorpusID:25771706

[7] S. Zeng et al., "Graphene–gold metasurface architectures for ultrasensitive plasmonic biosensing," *Adv. Mater.*, vol. 27, no. 40, pp. 6163–6169, 2015. [Online]. Available: https://www.researchgate.net/publication/281618671_Graphene-Gold_Metasurface_Architectures_for_Ultrasensitive_Plasmonic_Biosensing

[8] C. Pan et al., "Reconfigurable intelligent surfaces for 6G systems: Principles, applications, and research directions," *IEEE Commun. Mag.*, vol. 59, no. 6, pp. 14–20, Jun. 2021.

[9] S. S. Bukhari, J. Y. Vardaxoglou, and W. Whittow, "A metasurfaces review: Definitions and applications," *Appl. Sci.*, vol. 9, no. 13, p. 2727, 2019.

[10] R. Karasik, O. Simeone, M. Di Renzo, and S. S. Shitz, "Beyond Max-SNR: Joint encoding for reconfigurable intelligent surfaces," in *Proc. IEEE Int. Symp. Inf. Theory (ISIT)*, 2020, pp. 2965–2970.

[11] C. Huang, A. Zappone, G. C. Alexandropoulos, M. Debbah, and C. Yuen, "Reconfigurable intelligent surfaces for energy efficiency in wireless communication," *IEEE Trans. Wireless Commun.*, vol. 18, no. 8, pp. 4157–4170, Aug. 2019.

[12] J. Rao et al., "A novel reconfigurable intelligent surface for wide-angle passive beamforming," *IEEE Trans. Microw. Theory Techn.*, vol. 70, no. 12, pp. 5427–5439, Dec. 2022.

[13] L. Dai et al., "Reconfigurable intelligent surface-based wireless communications: Antenna design, prototyping, and experimental results," *IEEE Access*, vol. 8, pp. 45913–45923, 2020.

[14] A. Araghi et al., "Reconfigurable intelligent surface (RIS) in the sub-6 GHz band: Design, implementation, and real-world demonstration," *IEEE Access*, vol. 10, pp. 2646–2655, 2022.

[15] J. Jeong, J. H. Oh, S. Y. Lee, Y. Park, and S.-H. Wi, "An improved path-loss model for reconfigurable-intelligent-surface-aided wireless communications and experimental validation," *IEEE Access*, vol. 10, pp. 98065–98078, 2022.

[16] L. G. da Silva, P. Xiao, and S. A. Cerqueira, "A 2-bit tunable unit cell for 6G reconfigurable intelligent surface application," in *Proc. 16th Eur. Conf. Antennas Propag. (EuCAP)*, 2022, pp. 1–5.

[17] J. A. Hodge, T. G. Spence, and A. I. Zaghloul, "A reconfigurable intelligent surface using a 2-bit programmable metasurface for communications," in *Proc. IEEE Int. Symp. Antennas Propag. USNC-URSI Radio Sci. Meeting (APS/URSI)*, 2021, pp. 97–98.

[18] X. Pei et al., "RIS-aided wireless communications: Prototyping, adaptive beamforming, and indoor/outdoor field trials," *IEEE Trans. Commun.*, vol. 69, no. 12, pp. 8627–8640, Dec. 2021.

[19] P. Ratajczak, E. Séguenot, and D.-T. Phan-Huy, "Experimental demonstration of 3D reflected beamforming at Sub6Ghz thanks to varactor based reconfigurable intelligent surface," in *Proc. 2nd Int. Conf. 6G Netw. (6GNet)*, 2023, pp. 1–7.

[20] L. Zheng and Y. Zhao, "Generalized Snell's law and its verification by metasurface," in *Proc. Int. Conf. Innovative Mobile Internet Services Ubiquitous Comput.*, 2020, pp. 364–372. [Online]. Available: https://api.semanticscholar.org/CorpusID:219605128

[21] D. F. E. Rousseau, "Detailed derivation of the generalized Snell–Descartes laws from Fermat's principle," *Opt. Soc. America*, vol. 40, no. 4, p. 676, 2023.

[22] Q. Wu and R. Zhang, "Towards smart and reconfigurable environment: Intelligent reflecting surface aided wireless network," *IEEE Commun. Mag.*, vol. 58, no. 1, pp. 106–112, Jan. 2020.

[23] C. Balanis, *Advanced Engineering Electromagnetics*. New York, NY, USA: Wiley, 2012.

[24] O. Ozdogan, E. Bjornson, and E. G. Larsson, "Intelligent reflecting surfaces: Physics, propagation, and pathloss modeling," *IEEE Wireless Commun. Lett.*, vol. 9, no. 5, pp. 581–585, May 2020.
[25] Q. Wu, S. Zhang, B. Zheng, C. You, and R. Zhang, "Intelligent reflecting surface-aided wireless communications: A tutorial," *IEEE Trans. Commun.*, vol. 69, no. 5, pp. 3313–3351, May 2021.
[26] H. Guo, Y.-C. Liang, J. Chen, and E. G. Larsson, "Weighted sum-rate maximization for intelligent reflecting surface enhanced wireless networks," in *Proc. IEEE Global Commun. Conf. (GLOBECOM)*, 2019, pp. 1–6.
[27] J. Cifuentes, J. Osa, I. Barrutia, and M. Mendicute, "Towards affordable RIS devices: Electromagnetic simulation and implementation of metasurfaces," in *Proc. 14th Int. Symp. Commun. Syst., Netw. Digit. Signal Process. (CSNDSP)*, 2024, pp. 421–426.
[28] B. M. Brown, M. S. P. Eastham, and K. M. Schmidt, *Periodic Differential Operators: Floquet Theory*. Basel, Switzerland: Springer, 2013, pp. 1–29. [Online]. Available: https://doi.org/10.1007/978-3-0348-0528-5_1
[29] F. Costa and M. Borgese, "Electromagnetic model of reflective intelligent surfaces," *IEEE Open J. Commun. Soc.*, vol. 2, pp. 1577–1589, 2021.
[30] T. Roberts and D. Young, "Broadband device modeling and Q calculations of barium strontium titanate (BST) varactors," *Anritsu Tech. Bull.*, vol. 98, p. 1–6, Mar. 2023.
[31] T. Roberts and J. Martens, "Switching speed measurements of barium strontium titanate (BST) varactors," *Anritsu Tech. Bull.*, vol. 99, no. 32, pp. 1–6, Sep. 2024.

JOKIN CIFUENTES (Member, IEEE) received the Double degree in telecommunications systems engineering and computer science engineering from the University of Mondragon in 2019, and the master's degree in telecommunications systems engineering from the Polytechnic University of Madrid in 2021.

From 2022, he has been working on his Ph.D. thesis focused on RIS communications with the Signal Theory and Communications Group, Polytechnic School of Mondragon Unibertsitatea. His research interests include the design and fabrication of radiofrequency electronic systems, with a particular focus on metasurfaces and RIS structures.

IBAN BARRUTIA (Member, IEEE) received the degree in telecommunications engineering from UPNa, Pamplona, Spain, in 2003, with specialization in radiofrequency and microwave systems, and the Ph.D. degree in engineering from the University of Cantabria, Santander, Spain, in 2022, in the design, simulation, and measurement of monolithic microwave integrated circuits in gallium nitride.

Since 2015, he is a member of the Signal Theory and Communications Group, Polytechnic School of Mondragon Unibertsitatea. His topics of interest are radio frequency electronics systems and monolithic integrated circuits.

MIKEL MENDICUTE (Senior Member, IEEE) received the B.Sc., M.Sc., and Ph.D. degrees in electrical engineering from Mondragon Unibertsitatea, Mondragon, Spain, in 2000, 2003, and 2008, respectively.

He was with the Communications Area of Ikerlan Research Center from 1998 to 2003, where he worked on the development of communications devices and embedded systems. Since 2003, he has been with the Signal Theory and Communications Research Group, Department of Electronics and Computer Science, of Mondragon Unibertsitatea, where he is currently the Head of the Signal Theory and Communications Research Group. He was a Visiting Researcher with the Institute for Digital Communications, University of Edinburgh and also with the Telecommunications Circuits Laboratory, Swiss Federal Institute of Technology (EPFL) in 2004 and 2011, respectively. His current research interests include the design and implementation of digital signal processing algorithms for communications, monitoring and embedded systems with a focus on critical wireless communication interfaces for industrial and vehicular communications.